IOP Conf. Series: Earth and Environmental Science **49** (2016) 102007 doi:10.1088/1755-1315/49/10/102007

Dethridge wheel for pico-scale hydropower generation: An experimental and numerical study

Shakun Paudel[1] **and Nicole Saenger**[1]

[1]Department of Hydraulic Engineering, Faculty of Civil engineering, Darmstadt University of Applied Sciences, Haardtring 100, 64295 Darmstadt, Germany

E-mail: shakun.paudel@h-da.de, nicole.saenger@h-da.de

Abstract.

This study aims to assess the potential of the Dethridge wheel for developing power from very low head sites in open channel flow. The Dethridge wheel has been in use since early 20^{th} century for measuring flow in irrigation canals. Being robust and simple in design, this technology served as a reliable flow metering solution for more than a century. Working in a similar principle to the conventional waterwheel, this wheel could be a viable option of power generation for decentralized application in remote areas. Two different methods, experimental and numerical, are used for investigating the potential of the wheel. An experimental approach in which a physical model of the Dethridge wheel is built and tested at the hydraulics laboratory of Darmstadt University of Applied Sciences. Whereas a three dimensional numerical model of the Dethridge wheel is simulated using a commercial Computational Fluid Dynamics (CFD) code Flow-3D. Efficiency of around 60% is achieved in the model tests. Computed results are also in good agreement with the physical model results. The results from the physical and the numerical model are presented in this paper.

1. Introduction

The growing concern for the global climate change calls for an active switch to the renewable technologies for electricity production to reduce the greenhouse gas emissions [1]. Kyoto Protocol (1997) came into force to commit the industrialized countries to reduce emissions. Complying with the Kyoto protocol, the European Union directive 2009/28/EC has established a common framework for the use of renewable energy sources to limit the greenhouse gas emissions before 2020. These policies have placed much emphasis on renewable energy sources including hydropower. Hydropower represents a reliable source of renewable energy with majority of global renewable energy production contributing over 16% of the global electricity generation and accounting for 76% of total renewable electricity supply [2]. However, only a third of a total world hydropower capacity has been developed and most of this growth and development is concentrated in developed countries especially in Europe [2]. Large scale hydropower potential being mostly developed, the focus is now shifted to small scale hydropower. Within the small scale hydropower sector, very low head sites below 5 m, formerly disregarded considering uneconomical for developing hydropower [3], are recently getting renewed interest with governments providing subsidies to meet the renewable energy targets [4].

In order to develop these under utilised energy resources, conventional highly efficient low head hydraulic turbine technologies such as Kaplan or cross-flow turbines are not economically

viable because of the large size of the turbine required for very low head installations, requirement of special flow control mechanism and the risk they impose on the environment [5]. Furthermore, [6] reports that at current technologies and incurring costs, very small scale hydropower resources are not worth developing. Technological development is therefore required to harness this very low head energy potential. Efforts has been made to develop technologies that suitably harness the very low head energy source. Water wheels has been reassessed and optimised, for eg. see [7–10] and studies were undertaken to develop novel technologies such as hydrostatic pressure machine (HPM) [5, 11, 12], Very Low Head (VLH) turbine [13], the Archemedes screw [14] and Staudruckmachine [15] to name just a few. Although some developments have been made over the past few years, there still remains a potential for contributing towards the share of hydropower by developing technologies for utilising very low head sites.

The purpose of the present study is to identify the potential of the Dethridge wheel for harnessing power from very low head sites in open channel flow. The Dethridge wheel is a type of water wheel invented for measuring flow in the irrigation canals. John Dethridge introduced them in Australia in 1910. Until today, this machine, being robust and simple to use, is widely used in Australia for flow measurement purposes. Being similar in working principle to the conventional water wheels, this wheel is believed to have significant potential to be used for electricity generation from very low head sites. The hydraulics and performance characteristics of the laboratory scale Dethridge wheel model and numerical model study of the wheel in commercial Computational Fluid Dynamics (CFD) code Flow-3D are presented.

2. Experimental Set-up

The test rig comprised of pumps, overhead tank, pipelines, flow meter, a flume, and the tail race tank. The flume was rectangular, 20 m long, 1 m wide and 1.5 m deep and accommodated a model of the Dethridge wheel with shroud, shaft, torque transducer, speed sensor, stilling tubes, an inlet tank at the upstream and a control weir at the downstream. Side walls of the flume were made up of a glass and the bottom was a smooth concrete floor. The slope of the channel was horizontal (the bed slope was 0). The maximum flow rate the test set up could safely handle was around 35 l/s. Water was supplied through a pump of 50 l/s maximum capacity. General layout of the test rig is shown in Fig. 1.

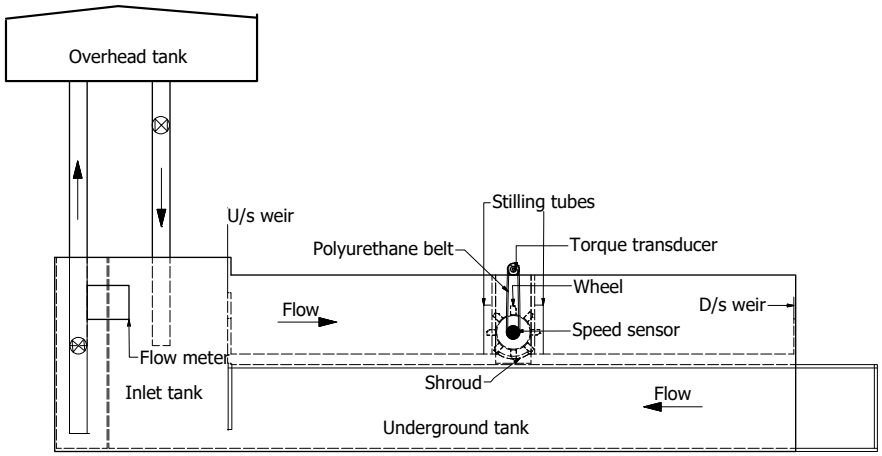

Figure 1: Schematic sketch of the test facility

The Dethridge wheel model consisted of a hub, blades and the side coverings. The model wheel was built in 1:2 scale to the original dimensions given in [16]. Original dimensions were in

FPS system, while converting to the SI system these dimensions were rounded off for practical purpose. The hub of the wheel was made up of PVC, which was 40 cm in diameter and 25 cm wide. The wheel was covered with a 20 mm thick PVC side covers on both sides to ensure the stability of the wheel and to avoid the accumulation of water inside the hub which would otherwise retard the wheel motion. Eight V-shaped steel blades of 2 mm thickness were mounted along the circumference of the hub. Blades were 10 cm long and were bent in V-shape to acquire an angle of 127 °. At the apex of each blade, an air vent was located to facilitate the filling and emptying of adjacent compartments as they enter and exit the water surface. The apex of the V is leading in the direction of rotation. Both sides of the blades were chamfered to match the fillets at the junction of the side walls and the floor. The gap between the sides of the housing and the wheel and the bottom gap were minimised to 1 mm. The wheel was placed over the curved shroud profile in order to minimize the clearance gap losses. The curvature of the shroud makes an angle of 70° to the wheel. In Fig. 2, the wheel and shroud is shown with the upstream and downstream water levels used in the tests. The water levels were kept fixed in order to be able to compare results between physical and numerical model. The physical model of the wheel is shown in Fig. 3.

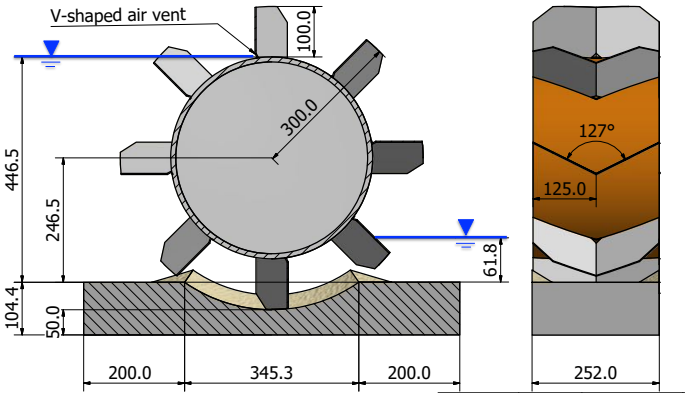

Figure 2: The wheel and the shroud (dimensions are in mm)

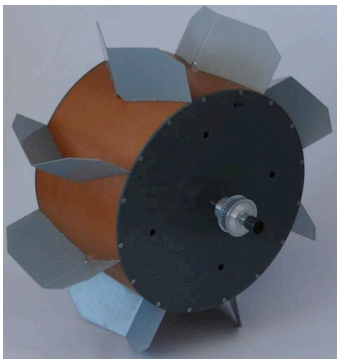

Figure 3: The physical model wheel

Flow rate delivered to the test flume was measured using a magnetic flow meter. This volumetric mass flow rate through the wheel control volume includes the amount of leakage flow through the side and bottom clearance gaps. The torque on the wheel shaft was measured using the torque transducer. The measured torque includes mechanical losses due to the bearings and the belt drive. The speed was measured using a solid shaft pulse encoder. The speed of the wheel was varied by applying load on the wheel through a hysteresis braking system.

The total head acting on the wheel is the difference between pressure and velocity heads at the inlet and outlet of the wheel. The elevation head is 0. Water levels were measured at the immediate upstream and downstream of the wheel control volume. To measure the water levels, two stilling tubes were installed and depth gauges were used for the manual reading of the flow depth values. The mean velocity of the flow is then calculated from the known area of flow and the flow rate ($v = Q/A$). The total head H is therefore given by,

$$H = \left(h_1 + \frac{v_1^2}{2_g}\right) - \left(h_2 + \frac{v_2^2}{2_g}\right) \tag{1}$$

The upstream water depth $h_1 = 44.65$ cm and the downstream depth $h_2 = 6.2$ cm were kept fixed in all the tests. The power output is calculated from the known values of speed of the

wheel (N) and the torque (τ) using Eq. 2. The measured power output (P_{out}) also includes the mechanical losses due to the bearings and the belt drive.

$$P_{\text{out}} = \omega\tau = \frac{2\pi N\tau}{60} \tag{2}$$

The mechanical efficiency of the wheel is the ratio of shaft power output and the hydraulic power input and is given by Eq. 3. This efficiency combines the hydraulic efficiency, volumetric efficiency of the wheel and the mechanical efficiency of the bearings and the belt drive system.

$$\eta = \frac{P_{\text{out}}}{P_{\text{in}}} = \frac{2\pi N\tau/60}{\rho QgH} \tag{3}$$

Output signals from all the measurement instruments were collected into a junction box and fed to a computer using a LabView based program. For each constellation, data was acquired for approximately one to two minutes and the mean value was taken for the analysis. The uncertainty in the measured data is calculated using constant odd combination method [17].

3. CFD Model

CFD commercial code Flow-3D (version 10.1.0.4) developed by Flow Science, Inc. was selected in this study. Flow-3D uses finite volume approach to solve the Reynolds-averaged Navier-Stoke's (RANS) equations over the computational domain. The computational domain is divided into a grid of variable-sized hexahedral cells. With each cell there are associated local average values of all dependent variables. For each cell values variables are solved at discrete times using a staggered grid technique [18]. The staggered grid places all dependent variables at the center of each cell except velocities and fractional areas, which are located at the center of the cell faces normal to the corresponding direction. Free surface of the flow is tracked using the Volume of Fluid (VOF) method developed by [19]. Solid body is defined as an obstacle by the implementation of the Fractional Area/Volume Obstacle Representation (FAVOR) method where obstacles are embedded in a fixed grid by allowing them to block portions of grid cell faces and cell volumes. The geometry is therefore conveniently represented within the grid cells [20]. The FAVOR method is a porosity technique to define obstacles. The grid porosity value is 0 within the obstacle and one for cells without the obstacle. Cells only partially filled with an obstacle have a value between 0 and one [21]. The RNG $\kappa-\varepsilon$ model was used for the turbulence modelling. A systematic CFD uncertainty evaluation process known as Grid Convergence Index (GCI) described in [22] is used for evaluating the uncertainties in the numerical model.

A 3D CAD model shown in Fig. 4 was prepared using Autodesk Inventor® 2014 from Autodesk, Inc and imported as STL files to be read and interpreted by Flow-3D. Taking the available computational resources and time into consideration, only the symmetrical half of the model was simulated. The 2 mm thick wheel blades, the complex geometry of the wheel and shroud combined with the nature of orthogonal meshing meant that very small cell sizes were required to resolve the complex geometry. The 2 mm blade thickness thus imposed a modelling challenge with a requirement of very fine meshing and consequently resulting in significantly longer simulation time. Therefore, the blades in the CAD model were thickened to 4 mm to achieve a required resolution. Ultimately, three nested mesh blocks of cell size 10 mm, 5 mm and 2.5 mm as shown in Fig. 5 were used to embed the geometry into the computational domain. The details of this mesh is summarised in Table 1. The origin $(0, 0, 0)$ is the center of the wheel. The nested meshing on the symmetrical half of the geometry allowed the area around the wheel to be refined and thereby reduced the computational effort to a great extent.

The boundary and initial conditions were defined to capture the physical processes. Volume flow rate was prescribed as inflow by creating a bottom inlet. At the downstream, pressure boundary condition with a stagnation pressure condition and prescribed fluid elevation was

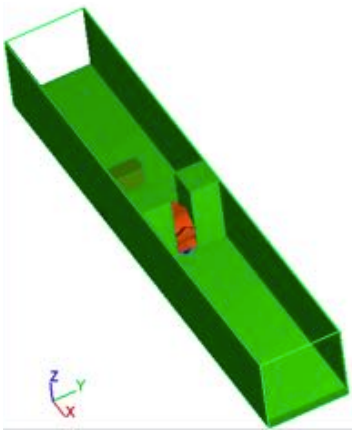

Figure 4: 3D Model

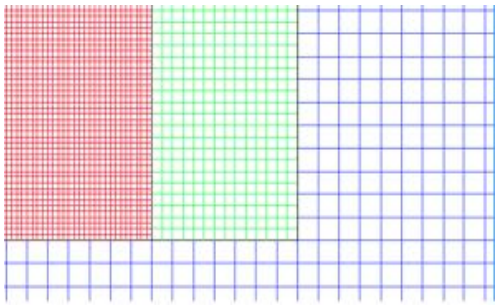

Figure 5: Nested meshing

Table 1: Mesh details

Block	Cell size (mm)	No. of cells
1	10	208000
2	5	201600
3	2.5	991440

defined. The sides of the domain and top boundary were defined as symmetry boundaries as fluid is not in contact at these boundaries. The fluid is in contact with the solid geometry of the model. A no-slip boundary condition was prescribed at all solid surfaces. The law of the wall was used to define the shear stress and the y^+ criteria ($30 < y^+ < 500$) was met in all cases. Uniform pressure distribution and fluid initialization with fluid elevation were used as initial conditions for the model. The fluid was defined as water at $20°C$ with a density of 1000 kg/m^3 and a dynamic viscosity of 0.001 Ns/m^2.

4. Results and Discussion

The wheel is partially submerged into water at normal operating condition. The upstream and downstream water levels are the determinants of the hydrodynamics of the wheel. The number of blades at work at any given time depends upon the depth of upstream and downstream water levels h_1 and h_2 respectively. The upstream water level depends on the flow rate, the rotational speed of the wheel and on the downstream water level. The downstream water level however varies very little with the speed of the wheel and the flow rate. The upstream and downstream water levels were kept fixed for all the tests ($h_1 = 44.65$ cm, $h_2 = 6.2$ cm) in order to be able to compare data with the numerical model results. The velocity head term in Eq. 1 is very small and therefore the total head acting on the wheel is dominated by the pressure head term. The measured data has shown that at constant water levels, the rotational speed of the wheel holds a linear relationship with torque as well as with the flow rate as shown in Fig. 6. Taking these linear models, full performance curves of the wheel are developed. In Fig. 6, the maximum power output (≈ 28 W) occurs around half of the stall torque. The Best Efficiency Point (BEP) is however at lower rotational speed of 11 rpm.

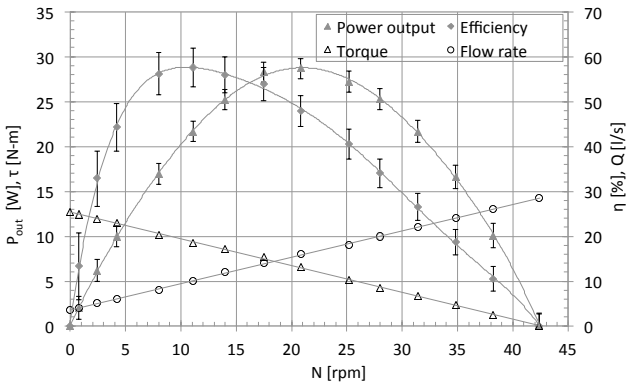

Figure 6: Power output, efficiency, torque and flow rate

These results are compared with the numerical model results. In the numerical model, two points referring different rotational speeds within the operating range are taken for the simulation. The torque, flow depths, total head and flow rates are acquired at the prescribed rotational speeds of $N = 7.97$ rpm and $N = 25.18$ rpm. The distribution of eight blades produces 45° angle between the two subsequent blades.

The velocity contours and vectors around the wheel at various angular positions of 0° to 45° revolution for the rotational speed of $N = 7.97$ rpm are shown in Fig. 7a-7f. The same cycle repeats as the rotational angle increases and completes one full revolution of the wheel in eight cycles. The flow field around the rotating wheel is complicated. The presence of the wheel creates a blocakage effect on the flow and the flow velocity becomes high at the wake of the wheel. At higher rotational speed, that is at higher flow rates, the flow field shows high amount of surface disturbance and large waves on the upstream and splashing and flow disturbance at the blade exit area at the downstream. The flow exhibits an oscillatory behaviour. The area at the inlet zone shows the region where the x-velocity is negative indicating the region of flow recirculation, separation due to the blade and flow interaction. As the blade completely intrudes into the water (Figures 7c and 7d), flow circulation and a vortex becomes clearly visible. This vortex continues to travel downstream until the next blade enters into the upstream water surface. The flow velocity within the cell continuously increases as it moves downstream. At the exit zone, another minor recirculation of the flow within the blade cell becomes visible. The flow velocity of the wake at the downstream of the wheel is obviously the highest. The flow velocity is in the range between -0.68 to 4.5 m/s with a maximum velocity occurring at an angular position of 37.42°. The recirculation of flow impacts the blade motion and contributes to the losses reducing the efficiency of the wheel.

The numerical model output at the rotational speed of $N = 7.97$ l/s is plotted in Fig. 8. The temporal development of main variables i.e., flow rate (Q), upstream flow depth (h_1), downstream flow depth (h_2), the total head (H) and the torque (τ) are monitored over the simulation time of 30 s. The mean value of these variables from 20 s to 30 s is calculated by using the smoothing spline model of the curve fitting tool in Matlab®. The outliers in the data are excluded in the fitted model and the mean and the standard deviation (σ_s) of the variables are computed and presented in Table 2.

The upstream free surface interaction with the wheel blades produce large fluctuations on the variables. The periodic evacuation of the blade cell at the exit and fluid displacement by the blade at the entry creates oscillation of the free surface and generate surface waves and pulsating loading forces on the wheel. As a result, the wheel experiences significant cyclic torque oscillations. These oscillations, if the amplitude is significant, could lead to structural damage of the wheel.

The wheel is simulated at another operating point of $N = 25.18$ rpm rotational speed. Two dimensional flow field at various rotational angles of $0° - 45°$ for $N = 25.18$ rpm are shown in Fig. 9a-9f. The contours show the x-velocity distribution. In comparison to the previous case, the higher speed of the wheel resulted in a substantial fluctuation on the upstream water depths with high amplitude upstream waves. This fluctuation on the water depth and the blade

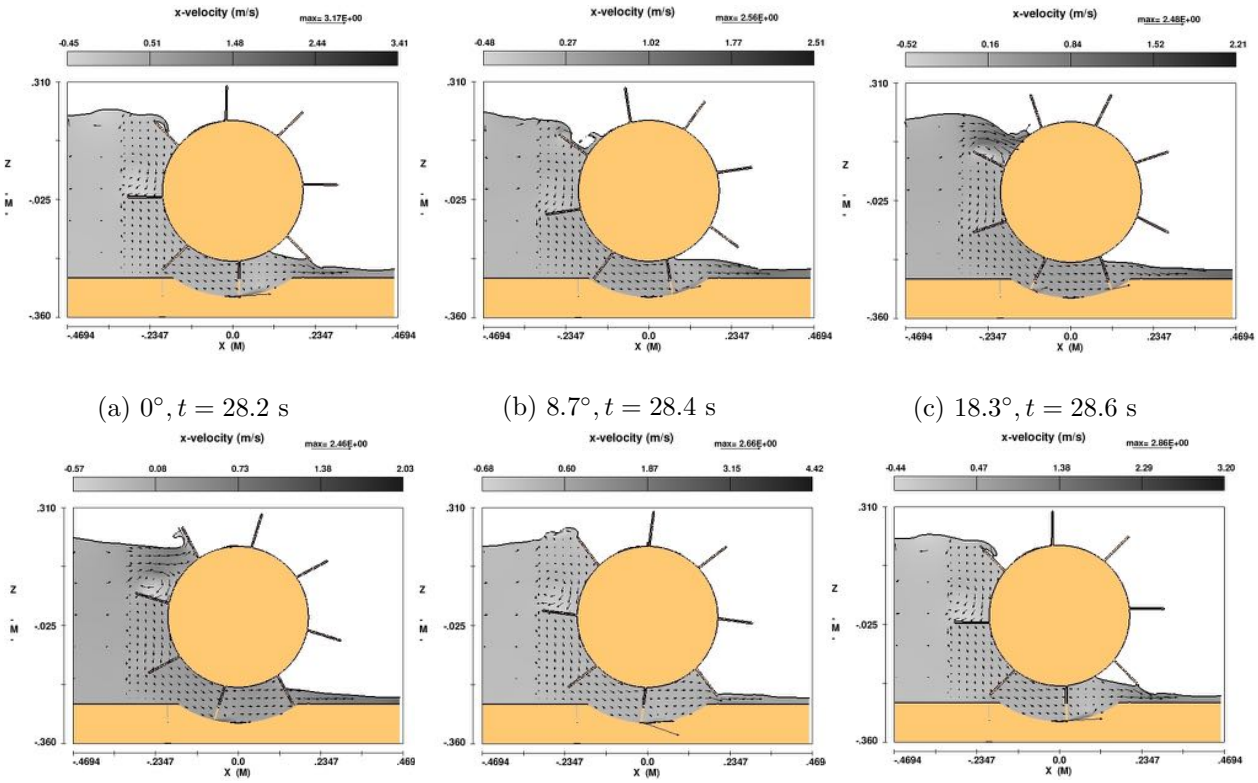

(a) $0°, t = 28.2$ s (b) $8.7°, t = 28.4$ s (c) $18.3°, t = 28.6$ s

(d) $27.85°, t = 28.8$ s (e) $37.42°, t = 29.0$ s (f) $45°, t = 29.15$ s

Figure 7: x-velocity contour and vectors for $N = 7.97$ rpm at different rotational angle. At every 45° rotation, new blade enters the water surface and the same cycle repeats. Flow is from left to right.

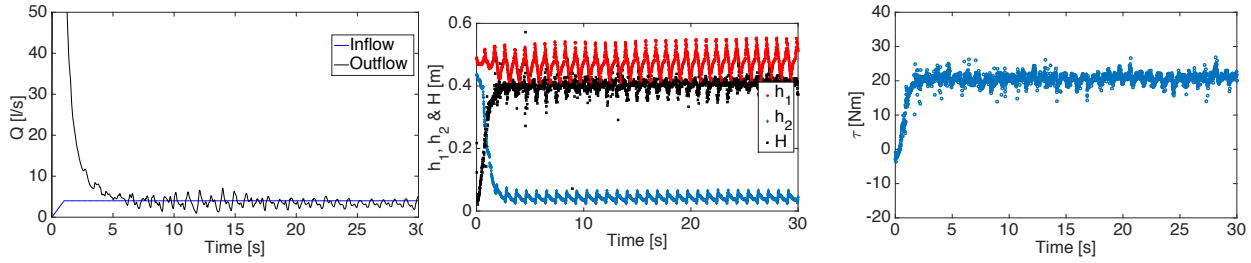

(a) (b) (c)

Figure 8: Model output for $N = 7.97$ rpm against simulation time. (a) Flow rates at inlet and outlet boundary; (b) Upstream and downstream water levels and the total head; (c) Total torque.

distribution around the rotational axis caused increased periodic loading on the wheel producing large amplitudes on the wheel torque. Fluid displacement caused by the entry of the blades is substantial as captured in Figures 9c and 9d. The formation of the vortex, flow separation and recirculation zone inside the blade cell is clearly noticed in Fig. 9b. The velocity distribution resulted in between -3.0 to 3.5 m/s.

Table 2: Numerical model output for $N = 7.97$ rpm

Parameter	Mean	$\pm\sigma_s$
Q (l/s)	6.93	$\pm$1.56
τ (Nm)	20.70	$\pm$1.19
h_1 (cm)	47.53	$\pm$3.48
h_2 (cm)	5.23	$\pm$0.80
H (cm)	40.45	$\pm$1.34

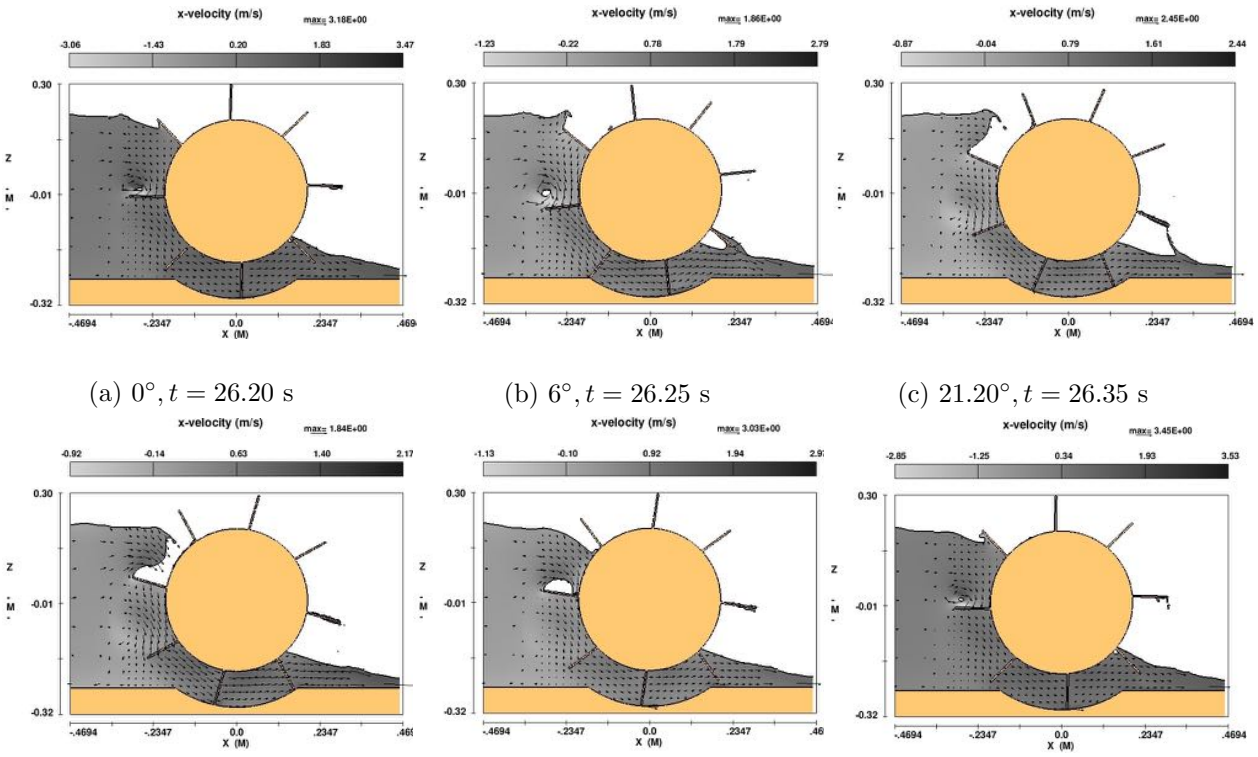

(a) $0°, t = 26.20$ s (b) $6°, t = 26.25$ s (c) $21.20°, t = 26.35$ s

(d) $28.74°, t = 26.40$ s (e) $36.30°, t = 26.45$ s (f) $45.35°, t = 26.50$ s

Figure 9: x-velocity contour and vectors for $N = 25.18$ rpm at different rotational angle. The change in the flow field between rotational angle of $0° - 45°$ is shown. Flow is from left to right.

The output of the main variables for $N = 25.18$ rpm are presented in Fig. 10. The simulation ran for 30 s and the mean was taken from 20 to 30 s of simulation time. These results show that the fluctuation of the variables about the mean value is significant at higher rotational speed as compared to the previous case of $N = 7.97$ rpm (see Table 2). The upstream water depth shows highest fluctuation with standard deviation of $\pm$3.90 cm. The mean value of the variables and their corresponding standard deviation for $N = 25.18$ rpm are summarised in Table 3.

As mentioned previously, at constant water depths the rotational speed and the torque as well as the rotational speed and the flow rate acquire linear relationship. By having equations of these linear models, the power output and efficiency at different rotational speeds is calculated. In Figures 11a and 11b, the numerical and physical model results are compared with corresponding uncertainties in both physical model and numerical model results. Although the numerical model over predicts both the power output and the efficiency at higher rotational speeds, the computed results lie within the defined uncertainty bounds around the BEP region and thus are in good

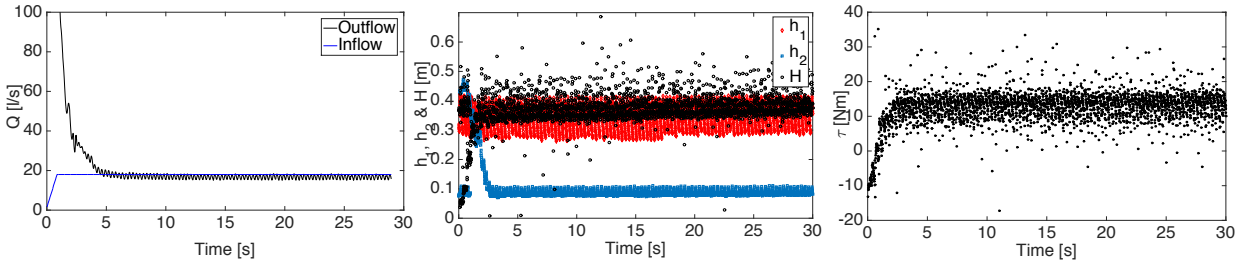

(a) (b) (c)

Figure 10: Model output for $N = 25.18$ rpm as a function of simulation time. (a) Flow rates at inlet and outlet boundary; (b) Upstream and downstream water levels and the total head; (c) Total torque.

Table 3: Numerical model output for $N = 25.18$ rpm

Parameter	Mean	$\pm\sigma_s$
Q (l/s)	16.79	$\pm$0.90
τ (Nm)	12.27	$\pm$2.27
h_1 (cm)	45.41	$\pm$3.90
h_2 (cm)	6.59	$\pm$0.73
H (cm)	37.98	$\pm$2.83

agreement.

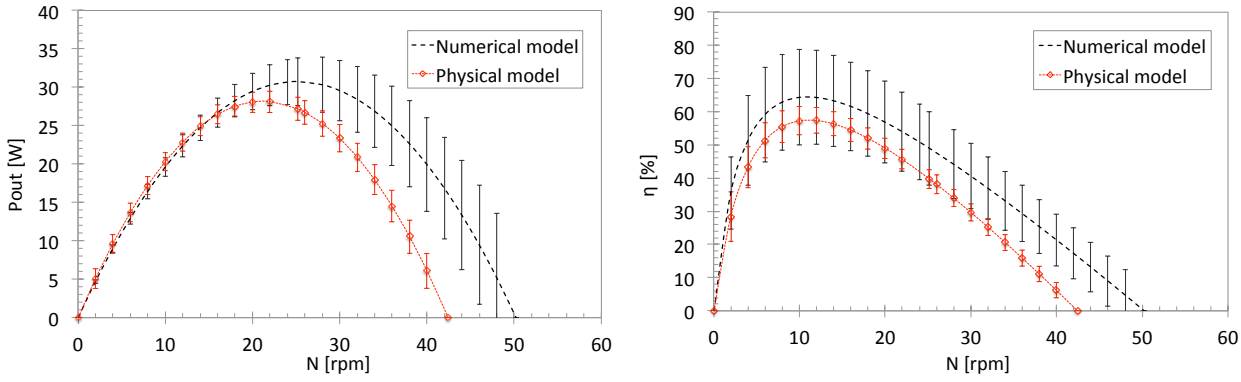

(a) (b)

Figure 11: Numerical and physical model results (a) Power output (b) Efficiency

5. Conclusion

In this paper, the Dethridge wheel was assessed for its potential for developing power from very low head sites in open channel flow using physical and numerical modelling approaches. Physical model tests have shown that at constant water levels the rotational speed of the wheel holds a linear relationship with torque as well as with the flow rate. Using these linear regression models, full performance curves of the wheel were developed. The physical model results of the wheel were compared with the numerical model results. The numerical model

was slightly over predicting the efficiency. However, the results were within the estimated uncertainty bounds around the BEP region. The numerical model results showed that CFD method could adequately predict hydrodynamic performance of the Dethridge wheel. Three dimensional hydraulics information from the CFD model provided the basis for qualitative analysis and visual examination of the flow field around the wheel and quantitative information on the wheel performance.

Based on the above results, we conclude that the Dethridge wheel is a potential device for energy extraction from very low head sites in open channel flow. The simple and robust design of the wheel in combination with the efficiency of around 60% achieved in the laboratory scale physical model tests could make this wheel a viable option for decentralised pico-scale hydropower generation from very low head sites in remote areas.

Acknowledgements
Authors would like to gratefully acknowledge the financial support from the German Ministry of Education and Research (BMBF) and the Schlumberger Foundation faculty for the future program.

References

[1] Sims R, Schock R, Adegbululgbe A, Fenhann J, Konstantinaviciute I, Moomaw W, Nimir H, Schlamadinger B, Torres-Martínez J, Turner C, Uchiyama Y, Vuori S, Wamukonya N and Zhang X 2007 *In Climate Change 2007: Mitigation. Contribution of Working Group III to the Fourth Assessment Report of the Intergovernmental Panel on Climate Change* ed Metz B, Davidson O, Bosch P, Dave R and Meyer L (Cambridge, United Kingdom and New York NY, USA: Cambridge University Press) pp 253–315

[2] World Energy Council 2015 World energy resources: Charting the upsurge in hydropower development 2015 Tech. rep. World Energy Council London, United Kingdom

[3] Müller G and Kauppert K 2002 *Proceedings of ICE, Civil Engineering* vol 150 pp 178–186

[4] Vowles A S, Karlsson S P, Uzunova E P and Kemp P S 2014 *Ecological Engineering* **69** 151–159

[5] Senior J, Saenger N and Müller G 2010 *Journal of Hydraulic Research* **48** 703–714

[6] Kosnik L 2010 *Energy Policy* **38** 5512–5519

[7] Denny M 2004 *European Journal of Physics* **25** 193–202

[8] Müller G and Kauppert K 2004 *Journal of Hydraulic Research* **42** 451–460

[9] Pelliciardi V 2015 *Journal of Applied Water Engineering and Research* **3** 157–165

[10] Quaranta E and Revelli R 2015 *Energy* **87** 315–325

[11] Linton N 2013 Ph.D. thesis University of Southampton

[12] Paudel S, Linton N, Zanke U C E and Saenger N 2013 *Renewable Energy* **52** 1–7

[13] Juhrig L 2011 *WasserWirtschaft* **10** 327–333

[14] Nuernbergk D and Rorres C 2014 *Wasserkraft & Energie* **3** 37–47

[15] Sternecker A, Ulm D and Kühnke T 2013 Wasserkraft-staudruckmaschine [In German] eP Patent App. EP20,110,738,388

[16] Kraatz D B and Mahajan I K 1975 Small hydraulic structures Tech. rep. Food and Agricultural Organization (FAO) of the United Nations Rome

[17] Moffat R J 1988 *Experimental Thermal and Fluid Science* **1** 3–17

[18] Versteeg H and Malalasekera W 2007 *An introduction to computational fluid dynamics* 2nd ed (Harlow, England: Pearson Education Limited)

[19] Hirt C and Nichols B 1981 *Journal of Computational Physics* **39** 201–225

[20] Hirt C and Chen K S 1996 *8th International Coating Process Science and Technology Symposium* (New Orleans, LA, USA)

[21] Hirt C 1992 Volume-Fraction techniques: Powerful tools for flow modeling Report FSI-92-00-02 Flow Science Santa Fe, NM

[22] Roache P J 1997 *Annual Review of Fluid Mechanics* **29** 123–160